JACS
JOURNAL OF THE AMERICAN CHEMICAL SOCIETY

Article

pubs.acs.org/JACS

Surface and Bulk Effects in Photochemical Reactions and Photomechanical Effects in Dynamic Molecular Crystals

Naba K. Nath,[†] Tomče Runčevski,[‡] Chia-Yun Lai,[§] Matteo Chiesa,[§] Robert E. Dinnebier,[‡] and Panče Naumov*[,†]

[†]New York University Abu Dhabi, P. O. Box 129188, Abu Dhabi, United Arab Emirates

[‡]Max Planck Institute for Solid State Research, Heisenbergstrasse 1, D-70569 Stuttgart, Germany

[§]Masdar Institute of Science and Technology, P. O. Box 54224, Abu Dhabi, United Arab Emirates

Supporting Information

ABSTRACT: The increasing number of reports on photomechanical effects in molecular crystals necessitates systematic studies to understand the intrinsic and external effectors that determine and have predictive power of their type and magnitude. Differential light absorption and product gradient between the surface and the bulk of the crystal are often invoked to qualitatively explain the mechanical response of crystals to light; however, the details on how this difference in photochemical response accounts for macroscopic effects such as surface modification, deformation, or disintegration of crystals are yet to be established. Using both bulk- and surface-sensitive analytical techniques, a rare instance of benzylidenefuranone crystals is studied here, and it is capable of several distinct types of photomechanical response including surface striation and delamination, photosalient effect (ballistic disintegration and motion), and photoinduced bending by dimerization. The results provide a holistic view on these effects and set the stage for the development of overarching theoretical models to describe the photomechanics in the ordered solid state.

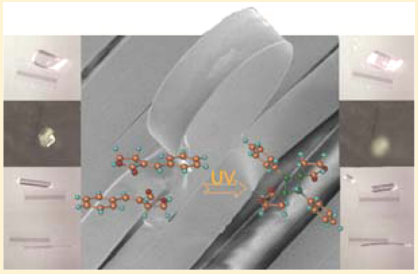

1. INTRODUCTION

The quest for efficient energy-transducing materials that could outperform polymeric actuators[1−4] has recently brought into the focus of solid-state chemistry research molecular single crystals that respond mechanically to photoexcitation. Depending on the response, the photomechanical effects in these dynamic crystals are manifested as bending,[5−13] curling,[14−16] twisting,[17−21] spinning, leaping, blasting,[6,22−28] and crawling.[29] We have proposed the collective term *photosalient effect* (PSE)[25] to demarcate a subset of these mechanical effects that appear as sudden light-induced locomotion whereby crystals leap many times their own size. The PSE is triggered by rapid release of internal strain that has been accumulated in course of a photochemical reaction, purportedly due to a secondary structure switching process such as a phase transition.[26] Unlike photoinduced bending, which has been observed with crystals of nearly all main photochemical classes (azobenzenes, anthracenes, diarylethenes, furylfulgides), the PSE is a rare phenomenon; since the first documented case of blasting crystals of α-santonin,[22,23] only a handful of instances have been reported that include processes such as electrocyclizations,[24] linkage isomerism,[25] and a few examples[7,26,27] out of the plethora of materials that are known to undergo [2 + 2] cycloaddition in the solid state.[30−41] Our personal communications with solid-state chemists over the past several years have added several new, previously unreported cases, indicating that the PSE and related effects are more common phenomena than it has been thought in the past. Regrettably, the serendipitous observations of the proclivity of crystals to deform, disintegrate, or explode are rarely reported, mainly because they have been considered a nuisance in routine X-ray (photo)diffraction analysis, thus remaining largely underexplored and unexplained. The need for solid materials for alternative energy transduction, however, has hastened this research field and several research groups have been particularly prolific in pursuing experimental and theoretical approaches to explain and to utilize these extraordinary phenomena.

Recently, some of us observed that crystals of one of the polymorphs of benzylidenedimethylimidazolinone (BDHI, Scheme 1) are capable of dual mechanical response;[7] while slender crystals exposed to even weak ultraviolet (UV) light slowly bend to more than 90°, thick crystals become PSE-active and hop violently off the base when excited with strong UV light. The multiple mechanical responses accessible with this material indicate that distinct mechanical response can be elicited in the same material, the type of mechanical effect being determined by intrinsic (crystal-related) factors, in addition to external factors such as the excitation energy and photon density. It is thus of interest to explore the conditions under which (elastic or plastic) *deformation* or (passive or ballistic) *disintegration* can be observed with the same material, in view of the fact that all these effects are alternative channels for relaxation of the elastic energy that has been accumulated

Received: July 26, 2015
Published: October 5, 2015

DOI: 10.1021/jacs.5b07806
J. Am. Chem. Soc. 2015, 137, 13866−13875

Scheme 1. Molecular structures of *E*-BDHF and *Z*-BDHF[a] and the related structures BDHI[b] and BBMO[c,d]

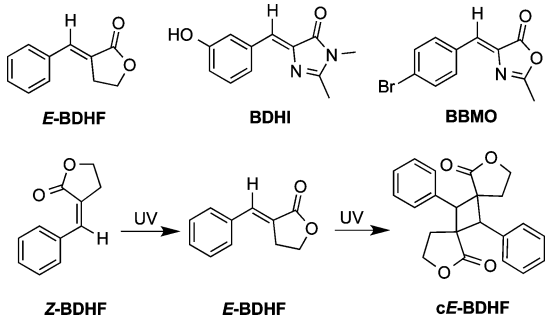

[a]3-Benzylidenedihydrofuran-2(3*H*)-one. [b]3-Hydroxybenzylidenedimethylimidazolinone. [c]4-(4-Bromobenzylidene)-2-methyloxazol-5(4*H*)-one. [d]The isomerization and dimerization reactions of *Z*-BDHF are shown at the bottom.

during the strain caused by structural transformation. Along this line of pursuit, we explored here 3-benzylidenedihydrofuran-2(3*H*)-one (BDHF), a molecule that can undergo $E \leftrightarrow Z$ isomerization as well as [2 + 2] dimerization similar to BDHI (Scheme 1). Kaupp and Haak showed that *Z*-BDHF can isomerize to *E*-BDHF in a crystal-to-crystal process.[42] Desiraju and Kearsley noted that upon exposure to UV light for several hours crystals of *E*-BDHF bend and crack, but they did not investigate the origin of these observations further.[43] Our own assessment of the reactivity of single crystals of BDHF exposed to UV excitation revealed highly incongruous mechanical response: though some crystals did not display any visible motility even at high excitation powers, others bent rapidly or burst violently. Being capable of multiple mechanical effects, this material appears ideally suited to investigate the relations between the intrinsic and external effectors on one hand and the mode of crystal actuation on the other. Here, in an attempt to disentangle the dependence of the response on these factors, we provide quantitative evidence that in addition to the crystal structure and properties of light excitation, the type of mechanical effect in molecular crystals is critically determined by their habit, size, and aspect ratio. The effects of the photochemical reaction on the surface adhesion force is also established by quantitative atomic force microscopy (AFM).

2. RESULTS AND DISCUSSION

2.1. Photomechanical Effects. A variety of crystal habits were obtained by recrystallization of *E*-BDHF from several solvents, including needles, plates, blocks, prisms, and layered twinned crystals (Figure S1, Supporting Information). The unit cells and crystal structures of crystals of all habits were identical with that of the *E* isomer. In a series of preliminary experiments, crystals of *E*-BDHF were subjected to excitation with continuous-wavelength (cw) polychromatic UV light from a medium-pressure Hg lamp (for details, see the Supporting Information). When exposed to UV light, the crystals hopped fiercely off the base (Figure 1a and b and Supporting Information Movie S1). Some crystals continued to move even after the excitation was terminated, indicating that the mechanical response is indirect consequence of the molecular changes that occur during the excitation or the ensuing photoreaction; instead, they appear as latent release of strain that has been accumulated during the photoreaction.

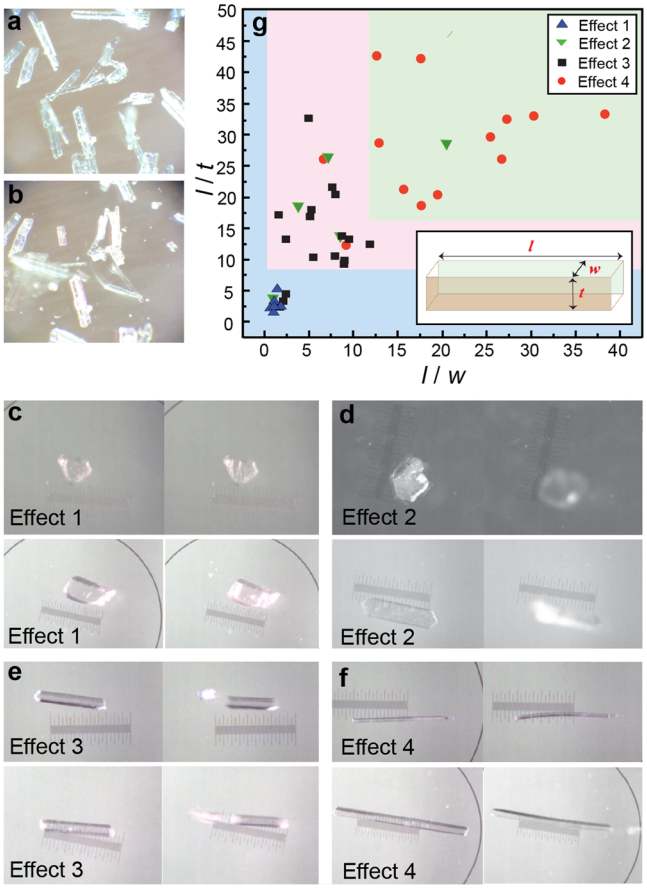

Figure 1. Photomechanical effects of *E*-BDHF. (a,b) Photosalient effect in crystals of *E*-BDHF excited with UV light shown before (a) and after (b) short exposure to UV light (video recording is available as Movie S1 in the Supporting Information). (c–f) Snapshots of the four kinematic effects observed during the photosalient effect of single crystals of *E*-BDHF (two examples are shown for each effect): cracking without motion (effect 1, c), hopping with preservation of macroscopic integrity (effect 2, d), splitting into fragments of nearly equal size that fly off (effect 3, e), and bending followed by breaking (effect 4, f). (g) Distribution of kinematic effects of *E*-BDHF over the crystal aspect ratio. The aspect ratio of crystals with size l (length) × w (width) × t (thickness) is presented as correlation between the ratios l/w (abscissa) and l/t (ordinate). The population of the upper half is not mirrored in the lower half due to the choice of the three dimensions ($l > w > t$), which implies $l/t > l/w$.

The UV-induced motion of the crystals was recorded with a high-speed camera operating at 4000 s^{-1} coupled to a microscope, and analyzed (Table S1, Supporting Information). The average in-plane speed of the debris was 0.01–2.19 ms^{-1}. These values are of the same order of magnitude with values that have been observed with systems that undergo PSE[25,26] and with the analogous thermally induced mechanical effect, that is, thermosalient effect (TSE).[44−46] Inspection of the recordings showed that the mechanical response is due to four kinematic effects that are shown as snapshots in Figure 1c–f (for video recordings, see Movies S2–S9, Supporting Information). Typically, the crystals either cracked while remaining still (effect 1; Figure 1c and Movie S2, Supporting Information), or they moved by displacement or hopping off the stage (effect 2; Figure 1d and Movies S3 and S4, Supporting Information). Some crystals split into two pieces that flew off in opposite directions (effect 3; Figure 1e and Movies S5–S7,

DOI: 10.1021/jacs.5b07806
J. Am. Chem. Soc. 2015, 137, 13866–13875

Supporting Information). Upon prolonged exposure to UV light the fragment(s) moved again without splitting or splintered violently (Movie S8, Supporting Information). Some crystals first bent, before they moved or split into two or several pieces that then flew apart from each other (effect 4; Figure 1f and Movie S9, Supporting Information).

Because the crystals are naturally sitting on their widest faces, the illuminated faces were $(\bar{1}01)$ and $(10\bar{1})$. The molecules near the exposed surface reacted, whereby the exposed face expanded due to stretching of the unit cell along the crystallographic *b* axis, which corresponds to the longest axis of the crystal (see below). In effect, the crystals always bent *away* from the direction of the incident light. Thicker crystals could not withstand the strain induced by the bending moment and responded by cracking, before they were propelled. Inspection of the morphology of the $(\bar{1}01)$ face by scanning electron microscopy (SEM) showed that the strain energy that has been accumulated over a long-range in the crystal was released by formation of cracks. When the elastic energy released by the reaction exceeded a threshold value, the crystals splintered and the excess energy was distributed as kinetic energy among the debris. The AFM images revealed increased roughness due to migration of matter on the crystal surface (Figure S2, Supporting Information).

2.2. Dependence of the Effect on the Crystal Aspect Ratio. We hypothesized that the photomechanical effects displayed by single crystals of *E*-BDHF depend on both intrinsic (e.g., crystal size, and resting face) and external factors (e.g., duration, direction, and wavelength and intensity of excitation). To study the effects of the crystal size on the PSE, 42 single crystals of varying aspect ratios were handpicked (twinned crystals or crystals with visible defects were prone to explosion and were excluded from analysis). The crystals, measured prior to exposure to light, were 0.19−2.80 mm long (*l*), 0.03−0.48 mm wide (*w*), and 0.02−0.24 mm (*t*) thick (Table S1, Supporting Information). As simple quantitative descriptors of the crystal habit, the aspect ratios l/w and l/t were calculated by approximating the real shape of each crystal with a rectangular block. Each of the crystals was in turn exposed to UV light on its $(\bar{1}01)/(10\bar{1})$ face for 1 min while keeping all other conditions identical. Figure 1g shows the distribution of kinematic effects over the two aspect ratios. The points corresponding to still crystals (7/42 crystals) are clustered around small aspect ratios. This result indicates that, at least under the experimental conditions used and the system studied here, it is not likely that photoreactive crystals having all three dimensions comparable to each other will be mechanically active. For higher aspect ratios, the crystals either split into pieces that fly off (effect 3, 17/42 crystals) or hop without splitting (effect 2, 5/42 crystals). Crystals that displayed effect 4 (bending followed by a photosalient effect, 13/42 crystals) were scattered toward higher aspect ratios. Thus, bending that precedes motility requires elongated crystals, such as prisms or, even more favorably, needles. These observations provide experimental support to the intuitive expectation that unconstrained long crystals are more likely to bend than thicker crystals, in line with some earlier results.[21] Furthermore, longer needle or platy crystals are expected to bend more compared to thicker or shorter crystals. Similarly, thicker crystals are expected to display PSE rather than to bend.

The preceding analysis indicated that bending requires high values of both aspect ratios, that is, bending is highly probable for long crystals. Our repeated and exhaustive attempts to obtain elongated crystals of *E*-BDHF by slow evaporation were unsuccessful. We then resorted to sublimation at 60 °C under reduced pressure. This method afforded elongated, layered crystals. When affixed at one end onto a glass fiber and exposed to UV light, these crystals bent until one part of the crystal broke off (Movie S10, Supporting Information). Twisting was observed when thin platy crystals were used. The type of deformation of small crystals (bending or twisting) could be controlled by adjusting the exposure time and power density (1−5% of the maximum power density of the 250 W Hg lamp). In some cases, upon continuous irradiation a layer separated off the crystal and subsequently bent (Figure S3 and Movie S11, Supporting Information) indicating that the surface layers of the crystal were delaminated (see the results in section 2.4 below).

2.3. X-ray Photodiffraction Analysis. The temporal course of the underlying photoreaction was followed by in situ high-resolution X-ray powder photodiffraction of *E*-BDHF powder irradiated with UV light (Figure 2a). Figure 2b shows

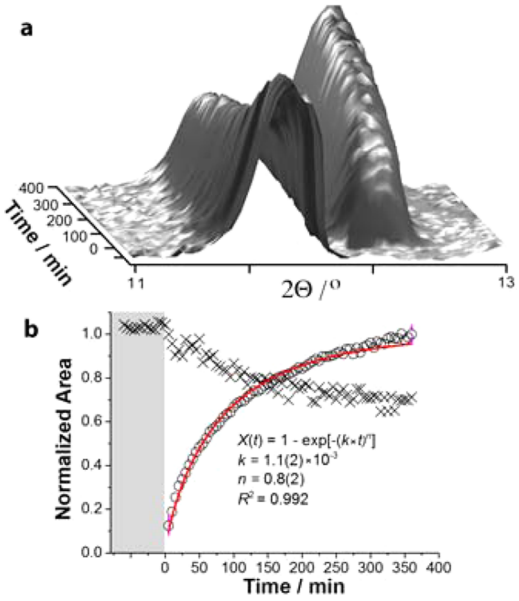

Figure 2. Monitoring of the photodimerization by in situ X-ray powder diffraction. (a) Time-profile of the scattered X-ray intensity of UV-irradiated *E*-BDHF. (b) Evolution of the normalized intensity of the (101) reflection of the reactant (*E*-BDHF, ×) and the product (c*E*-BDHF, ○). The red curve in panel b is a fit to the JMAK model and the gray area demarcates the dark period (before the UV irradiation).

the time-profile of the normalized intensity of the emerging (101) reflection of the product, c*E*-BDHF ("c" stands for "cyclo"). In spite of the scatter of the data introduced by technical limitations and decreased crystallinity, the evolution of the product fit the JMAK model well.[47−49] The Avrami coefficient, which is related to the dimensionality of the process, was $n = 0.8(2)$, revealing negative dimensionality, indicative of a negative autocatalytic step.[50] This behavior could be an artifact of the reduced crystallinity related to cracking of the microcrystals. Under these conditions, the presence of microdomains can effectively inhibit the nucleation growth of the product phase. Indeed, preliminary ex situ single crystal X-ray photodiffraction experiments where the reaction was

DOI: 10.1021/jacs.5b07806
J. Am. Chem. Soc. 2015, 137, 13866−13875

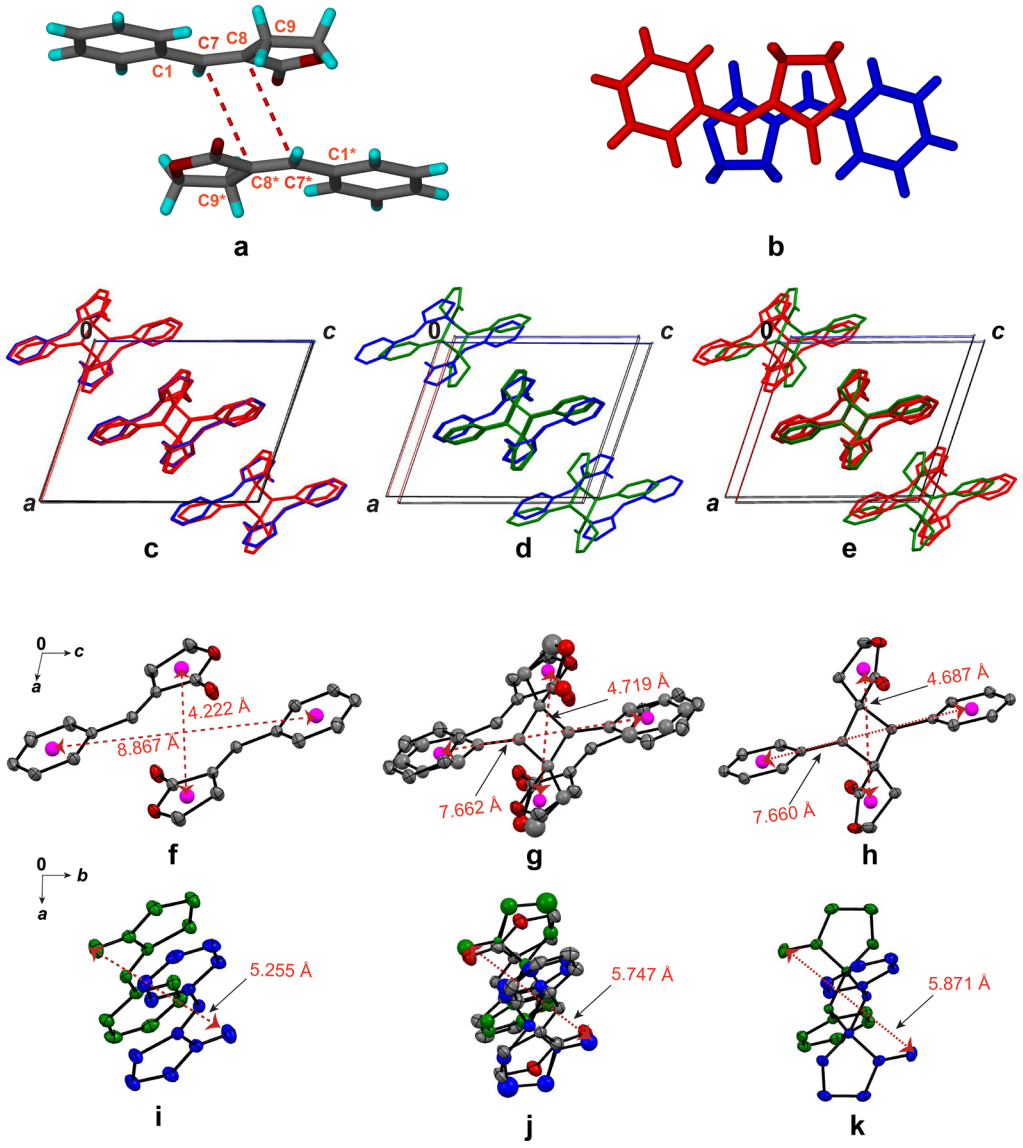

Figure 3. Geometrical criteria and mechanism of photodimerization in photosalient crystals of *E*-BDHF. (a) Definition of geometrical parameters that determine the reactivity for [2 + 2] cycloaddition in *E*-BDHF: θ_1 = ∠(C7C8C7*) = 110.2° and θ_2 = ∠(C7C8C7*C8*)-(C1C7C8C9) = 78.6°. (b) Relative disposition of the two inversion-related molecules of *E*-BDHF viewed normal to the molecular plane. (c–e) Overlaid representation of the packing diagrams shows the similarity in the structure of *E*-BDHF (blue), $(E\text{-BDHF})_{0.875}(0.5c E\text{-BDHF})_{0.125}$ (red), and crystal of pure c*E*-BDHF (green). (f–k) Changes in molecular geometry of *E*-BDHF during photodimerization (f–h, view along the *b* axis; i–k, view along the *c* axis). The centroids of the benzene ring and the γ-butyrolactone ring are shown in magenta. Disposition of the adjacent inversion-related molecules in *E*-BDHF (f, i), $(E\text{-BDHF})_{0.875}(0.5c E\text{-BDHF})_{0.125}$ (g, j), and c*E*-BDHF (h, k). In panels i–k, the atoms of the adjacent molecules in *E*-BDHF that are related by inversion, the two halves of the minor component in $(E\text{-BDHF})_{0.875}(0.5c E\text{-BDHF})_{0.125}$ and the two halves in c*E*-BDHF are shown in different colors.

conducted by exposing *E*-BDHF crystals to heat-filtered cw light from a medium-pressure UV lamp showed that the crystals had developed visible cracks and eventually disintegrated. Although the pieces obtained by disintegration still diffracted X-rays, the quality of the diffraction was insufficient for structure refinement by using single crystal diffraction data.

To retain the crystal integrity, a single crystal of *E*-BDHF of good quality was exposed to weak light from a set of LEDs (λ_{ex} = 365 nm) for 24 h (note that the crystals are colorless, and due to the overlap of the absorption bands in the UV region, the molar absorption coefficient and the penetration depth could not be determined). The crystal did not display any apparent surface defects. Determination of the crystal structure revealed that about 12.5% of the crystal was converted to the cyclobutane dimer (c*E*-BDHF). The ratio of the reactant and the product based on the refined site occupancy of the cyclobutane carbon atoms was 0.8753(18)/0.1247(18). Further irradiation of the mixed crystal, $(E\text{-BDHF})_{0.875}(0.5c E\text{-BDHF})_{0.125}$, for 24 h caused deterioration of its quality, which thwarted structure determination with single crystal X-ray diffraction. However, the resulting polycrystalline sample was amenable to structure analysis by X-ray powder diffraction (see below). To provide additional evidence of the chemical structure of the product, *E*-BDHF was irradiated for 5–10 min with high-power UV light and recrystallized from toluene. Crystals of the pure dimer c*E*-BDHF were obtained and their structure was confirmed with single crystal X-ray diffraction analysis. Comparison of the structure of the product c*E*-BDHF

DOI: 10.1021/jacs.5b07806
J. Am. Chem. Soc. 2015, 137, 13866–13875

Table 1. Unit Cell Expansion and Contraction during the Photodimerization of *E*-BDHF to c*E*-BDHF

parameter	*E*-BDHF	partially converted crystal[a]	relative change/%	c*E*-BDHF	relative change/%
a/Å	10.938(5)	11.011(3)	+0.67	11.769(4)	+7.59
b/Å	5.933(3)	5.9502(16)	+0.29	6.0891(19)	+2.63
c/Å	14.230(6)	14.085(4)	−1.02	12.403(4)	−12.84
β/°	108.714(6)	108.736(5)	+0.02	108.842(5)	+0.12
V/Å^3	874.6(7)	873.9(4)	−0.08	841.2(5)	−3.82

[a] $(E\text{-BDHF})_{0.875}(0.5cE\text{-BDHF})_{0.125}$.

with the structures of the unreacted crystals and the partially reacted crystal (Table S2, Supporting Information) showed a great similarity. Rietveld analysis of the in situ obtained product proved that it has identical crystal structure with the recrystallized dimer (Figure S4, Supporting Information).

Photoinduced [2 + 2] cycloaddition requires the distance between the reactive double bonds to be shorter than 4.2 Å, parallelism of double bonds, and minimal translation of the molecules in the crystal.[51] From the crystal structure of *E*-BDHF (Figure 3a and b), it is evident that the reactive double bonds of the nearest inversion-related molecules are not positioned ideally, although they are parallel with a center-to-center distance of 3.601(2) Å, a value that is well within the topochemical limits. The obtuse angle of the parallelogram defined by the double bonds (Figure 3a), a measurable of the displacement of the molecules along the double bond axis, is θ_1 = 110.11(6)° (ideal π-overlap requires 90°). The displacement of the double bonds in the molecular plane, as measured by the angle between the least-squares planes connecting the two double bonds and the least-squares plane parallel to the double bond, is θ_2 = 76.49(6)° (perfect π-overlap requires 90°). Thus, [2 + 2] dimerization in the crystal lattice of *E*-BDHF requires lateral displacement of the adjacent inversion-related molecules in the direction of the double bonds as well as perpendicular to it.

For comparison, in the crystal of the nonreactive isomer *Z*-BDHF the center-to-center distance between the two nearest parallel double bonds is 5.319 Å, and the two angles are θ_1 = 150.3° and θ_2 = 87.2°.[42] The inertness of the *Z*-isomer can also be explained on purely steric grounds, by comparing the volumes of the reaction cavities[52,53] around the reactive molecules in crystals of *Z*- and *E*-BDHF (Figure S5, Supporting Information; note that the term "reaction cavity" in this context refers to the available volume about a reactive molecule in its crystal lattice, whereas partial reaction cavity[53] is the available volume about a specific portion of the reactive molecule). However, a molecule of *Z*-BDHF could rotate inside the crystal lattice to isomerize to *E*-BDHF because it is confined to a cavity of considerably larger volume (65.57 Å^3) relative to *E*-BDHF (57.35 Å^3). The volumes of the partial reaction cavities of the benzene and γ-butyrolactone rings are in support of these conclusions. In *Z*-BDHF, the partial reaction cavity volumes of the benzene and γ-butyrolactone rings are 23.49 Å^3 and 24.16 Å^3, respectively, whereas in *E*-BDHF they are 22.29 Å^3 and 18.08 Å^3.

Overlapped models of the structures of the pure reactant, product, and partially converted crystal are shown in Figure 3c–e, and the unit cell changes are summarized in Table 1. In the partially converted crystal, the *a* and *b* axes expanded (+0.67% and +0.29%), whereas the *c* axis shrunk (−1.02%), resulting in negligible volume change (−0.08%) relative to the crystal before the reaction. However, despite the very similar packing structures of the dimer in the partially converted crystal and in the pure crystal (see above), relative to the pure reactant the *a* and *b* axes in the crystal of the pure dimer are longer, for +7.59% and +2.63%, respectively, whereas the *c* axis is much shorter, − 12.84%. The volume of the unit cell of the dimer is notably smaller (−3.82%). The pronounced difference in the unit cell parameters may be an indication of a phase transition that occurs after a critical amount of the product phase has been accumulated in the crystal; however, this assumption requires additional experimental verification.

The distortion of the unit cell can be explained by the molecular changes that occur in the course of the reaction (Figure 3f–k). The contraction of the *c* axis is related to the decrease in the intercentroid distance between the two adjacent benzene rings on going from pure *E*-BDHF (8.868(4) Å) to $(E\text{-BDHF})_{0.875}(0.5cE\text{-BDHF})_{0.125}$ (7.662(2) Å) and c*E*-BDHF (7.660(2) Å). Similarly, the expansion of the *a* axis can be explained by considering the intercentroid distance between the γ-butyrolactone rings of the adjacent, inversion-related molecules in *E*-BDHF (4.222(2) Å), and the product in $(E\text{-BDHF})_{0.875}(0.5cE\text{-BDHF})_{0.125}$ (4.719(2) Å) and c*E*-BDHF (4.687(1) Å). The expansion of the *b* axis can be explained by considering the distance between the carbonyl oxygen atoms, which changes from 5.255(2) Å in *E*-BDHF to 5.747(1) Å in $(E\text{-BDHF})_{0.875}(0.5cE\text{-BDHF})_{0.125}$ to 5.871(1) Å in c*E*-BDHF.

The solid-state photodimerization of a related compound, (*Z*)-4-(4-bromobenzylidene)-2-methyloxazol-5(4*H*)-one (BBMO, Scheme 1), was recently explained[54] as a three-stage process: photoexcitation, [2 + 2] dimerization accompanied by minimal geometrical changes, and phase transition where the atoms move in an organized manner relative to their neighbors, similar to the martensitic phase transitions.[44] We posit that the PSE in *E*-BDHF and similar compounds is also triggered by a phase transformation, which is accompanied by large change in the unit cell parameters. The latent mechanical response where some of the crystals continue to hop even after the UV irradiation has been terminated lend further experimental support to this hypothesis. Although with *E*-BDHF we could not detect a phase transition at *E*-BDHF/c*E*-BDHF ratio of up to 0.875/0.125, such transition cannot be excluded at higher yields. Collective molecular rearrangement requires sufficient amount of the dimer to be accommodated into the crystal lattice of the monomer. The requirement of a threshold amount for occurrence of the crystal blast is in line with the assumption of collective molecular movement.

The PSE is a highly stochastic process. In addition to measurable properties, such as is the crystal size, its occurrence is also determined by unpredictable or hardly detectable and predictable factors, such as is the presence of defect sites. Although all crystals used in this study were single crystals, defects, which are always present in real crystals either as a result of the crystallization or because they have been introduced by the history of the sample, could always lead to

DOI: 10.1021/jacs.5b07806
J. Am. Chem. Soc. 2015, 137, 13866−13875

premature explosion, before the actual stress for the effect has been accrued). We have recently shown that in the related TSE,[44] twinned crystals undergo the salient effect at lower temperature, because the twinning plane acts like a defect surface. The probability of having defect-induced ballistic event happen increases with crystal size. In view of these considerations, the 12.5% conversion could be taken as the *lower limit* for the occurrence of the effect in good single crystals of the size used in this study, that is, it takes at least 12.5% yield on average (throughout the crystal volume) to induce the effect. The actual onset of the fracture will also be affected by the conditions of the irradiation (intense light source versus weak light source) and the spatial distribution of the product inside the crystal (uniform vs localized distribution).

2.4. Surface Effects. Inspection of the surface morphology of the $(\bar{1}01)/(10\bar{1})$ face after dimerization by SEM showed that after the reaction the originally smooth surface (Figure 4a) has split in relatively uniform strips by cracks that run parallel to the longest side of the crystal, which coincides with the crystallographic *b* axis (Figure 4b). These cracks were on average 1.3(4) μm wide and were confined near to the surface

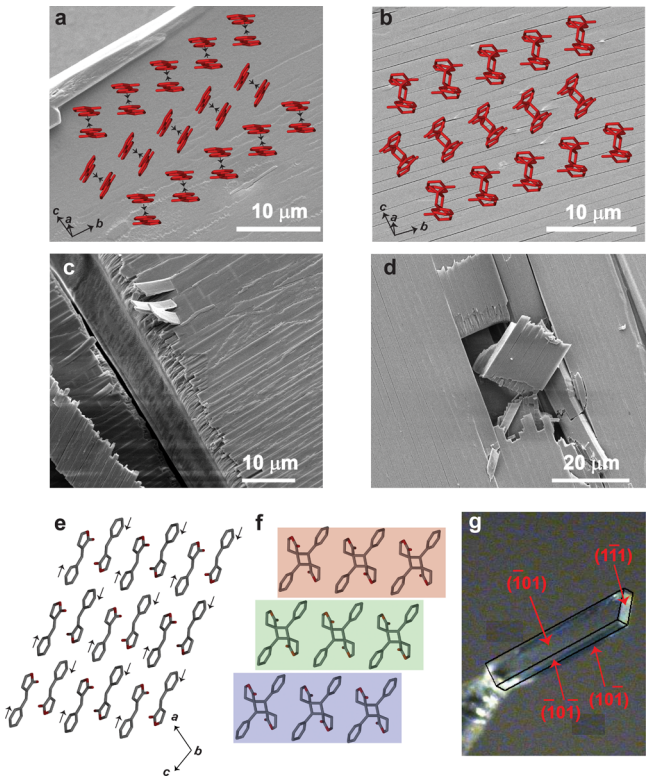

Figure 4. Changes in surface morphology during irradiation and relation with crystal packing. (a) Orientation of the molecules of *E*-BDHF on the $(\bar{1}01)/(10\bar{1})$ face before UV irradiation. The black arrows represent the direction of molecular movement during dimerization. (b) Dimerization by exposure to UV light (3 s) causes development of parallel, uniform cracks. (c) Cracking is followed by splitting of the crystal perpendicular to the direction of the parallel cracks. (d) Shrinking of the cracked layers causes delamination from the crystal. (e) Orientation of the molecules viewed through the *b* axis. The arrows indicate the direction of molecular movement during the reaction. (f) Layers of dimerized molecules that cause evolution of deep recesses and splitting of the crystal. (g) Face indices of a typical (nonreacted) crystal of *E*-BDHF.

of the crystal (see below). The molecular packing along the *b* axis is composed of tapes of monomer pairs (Figure 4a and Supporting Information Figure S7). As the molecules within the pairs come closer to each other during dimerization, the molecular tapes contract uniaxially in response to the contraction of the unit cell (see above). Because of the absorption of UV light, the reaction is limited to the crystal surface and the dimerization does not proceed throughout the crystal depth, the cracks evolve due to contraction of the tapes, whereby thin strips are formed close to the surface. These strips became clearly visible by aging of the sample in the SEM chamber over 2 days, whereby they curled up and delaminated off the crystal (Figure S6, Supporting Information). Being limited to the surface, these cracks do not contribute directly to the PSE, but they could play an important role in the (irreversible) bending of the crystal.

A second set of only a few albeit much deeper cracks were observed perpendicular to the strips (Figure 4c,d) When viewed along the *b* axis, the centrosymmetric pairs of molecules are arranged as layers (Figure 4e). The molecules within each pair undergo lateral movement toward each other. In effect, the layers contract, generating cumulative strain that leads to development of several recesses that protrude deep inside the crystal. These cracks are detrimental to the crystal integrity, causing splitting of the crystal along the diagonal between the *a* and *c* axes (Figure 4c) and separation of pieces (Figure 4d). We conclude that ultimately the anisotropy in the strain distribution during the photoreaction determines the type of the mechanical response, accounting for bending of slender crystals and occurrence of salient effects in case of thicker crystals.

2.5. Quantification of the Photoinduced Changes of Surface Properties. The photoinduced delamination is caused by the different behavior of the bulk and surface in the course of the photoreaction. Qualitatively, it can be explained by different degrees of strain anisotropy; though the material shrinks along three directions in the bulk, the shrinking at the surface is restricted to a plane (two directions). Thus, the shear forces in the crystal of *E*-BDHF are significant, and the system departs strongly from the model of planar stress state in the elasticity theory (within the planar stress state model, a physical body can ideally be described as a set of parallel slices that can be stretched only within their plane with negligible interplanar shear). The deformation of the surface is related to changes in surface energy (γ) that can be calculated from the force of adhesion (F_{AD}), that is, the maximum attractive force that an AFM tip experiences when it interacts with the sample (Figure S8, Supporting Information). F_{AD} is defined as the force when the tip is at the smallest distance between two bodies before a contact is established and the force between them becomes repulsive. The relationship between the surface energy and F_{AD} is obtained by invoking the sphere-and-a-flat-plane model[55,56]

$$F_{AD} = 4\pi R\gamma \quad (1)$$

where *R* is the radius of the sphere (i.e., the radius of the AFM tip).

As explained above, during the exposure to UV light, the surface of the *E*-BDHF crystal underwent apparent morphological changes (Figure 5a and b). Cracks appeared in effect to the tendency of the crystal to relax the differential anisotropy between the surface and the inner layers. To study the changes in surface energy, over 1000 force curves were recorded by in

DOI: 10.1021/jacs.5b07806
J. Am. Chem. Soc. 2015, 137, 13866−13875

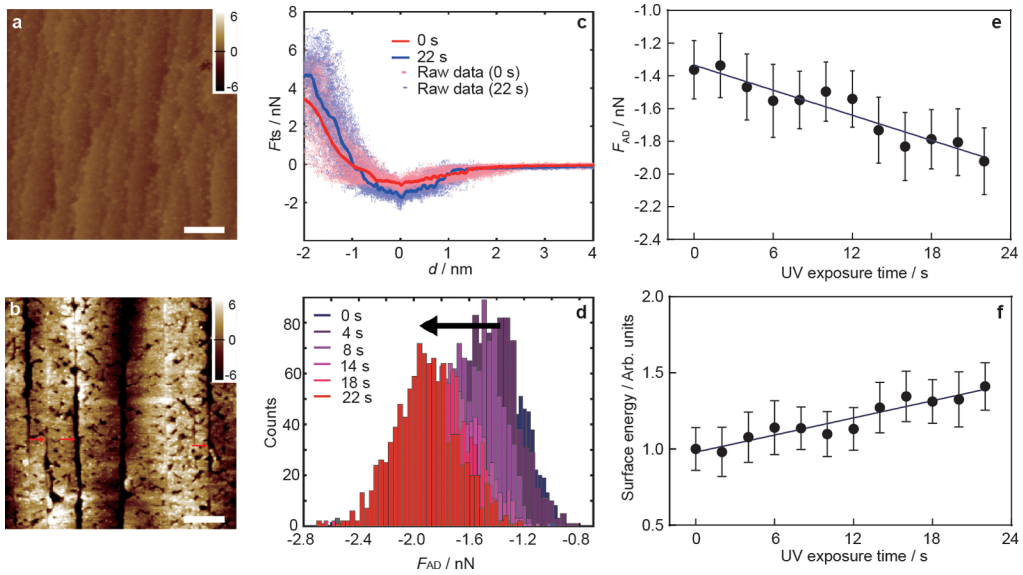

Figure 5. AFM study of the change of surface properties induced by UV light. (a, b) Typical AFM images of the surface of the *E*-BDHF crystal before (a) and after (b) 8 s exposure to UV light from a medium-pressure Hg lamp. The red arrows in panel b indicate the cracks that appear after UV irradiation. The scale bars correspond to 500 nm. (c) Averaged force curves before (0 s) and after 22 s of exposure to UV light shown together with a scatterplot of the raw data. F_{ts} stands for the tip−sample interaction force. (d) Distribution of the force of adhesion (F_{AD}) with exposure time. (e, f) Variation of the average force (e) and surface energy (f) with exposure to UV light. Point t = 0 s corresponds to the surface before the exposure, and the last data point was taken at t = 22 s after the onset of UV irradiation.

situ AFM before and at regular time intervals (2 s) during a total exposure time of 22 s. At each time point, 1000 curves were averaged within 20 min to account for artifacts. Two exemplary force curves, recorded at t = 0 s (before exposure to UV light) and at t = 22 s are shown in Figure 5c (the respective results from the individual measurements of F_{AD} were deposited as Figure S9, Supporting Information). The results showed that the main difference in the average curves is their depth, which is the maximum attractive force, F_{AD}, between the AFM tip and the crystal.

Figure 5c also illustrates change in the elastic modulus during exposure to UV light, in line with the different degree of anisotropy at the surface and in the bulk of the crystal. From the tip−sample force (Figure S8 Supporting Information) and the Dejarguin−Muller−Toporov (DMT) theory, the effective elastic modulus (E_{eff}) can be related to the slope of the curve when d < 0.[55−57] Assuming that the change due to UV absorption happens at the surface and recognizing that the stiffness measurement from the force−distance profile is representative for the first few nanometers of the material, the difference between the elastic moduli is in accord with the strong anisotropy hypothesis, yielding an increase of stiffness of ∼9% as a consequence of the photoreaction. This result is in line with the value (12%) obtained by Karunatilaka et al. by AFM nanoindentation.[58] However, the approach[59] used here has the advantage of providing *quantitative* changes in surface chemistry due to UV exposure by representation of the evolution of the force of adhesion, F_{AD}. Figure 5d depicts a histogram of the evolution of the F_{AD} distribution with exposure time. It is concluded that with UV exposure the population of F_{AD} shifts to lower negative force. This observation is due to the increasing population of dimerized product in the mixture with the reactant monomer, in line with the other results. The increase of the absolute value of F_{AD} suggests that after dimerization, the surface becomes more attractive for adsorption. In other words, the increase in $|F_{AD}|$ by illumination translates into stronger affinity of the surface of the crystal for the AFM tip due to stronger adhesion force. After averaging, this increase in affinity reflects the increasing ratio of the dimer molecules on the crystal surface.

Figure 5e shows the variation of the average F_{AD} as a function of the exposure time. Because it is well known that the tip radius R significantly affects the interaction between the tip and the sample surface, R was monitored in situ throughout the experiment using the critical amplitude method[60] that accounts for the apparent changes in R. The progressively different and statistically significant average of multiple measurements provided evidence that the changes in F_{AD} are not experimental artifacts[61] and that the absolute value of the adhesion force increases with exposure time (the negative sign is related to the attractive nature of the force). The surface energy γ calculated using eq 1 is plotted in Figure 5f (due to the uncertainty in determination of the exact size of the tip R, γ was normalized by its value before the UV irradiation). Figure 5f shows a 30% increase in the surface energy during the photodimerization. This increased surface energy is likely to be the cause of the changes that lead to the observed surface phenomena as well as the reason behind the appearance of cracks on the crystal surface. These cracks normally serve as nuclei for deeper fractures which ultimately account for the crystal disintegration.

3. CONCLUSIONS

In conclusion, a rare instance of photoreactive material that undergoes several photomechanical effects upon irradiation due to [2 + 2] photodimerization, including salient effects (PSE), macroscopic bending and surface changes (striation and delamination) was studied to establish semiquantitative correlations between the type and intensity of the mechanical effect, on one hand, and the changes in the bulk structure of the crystal and of its surface structure, on the other. The photoinduced changes in the bulk were established from photodiffraction experiments, whereas the changes in surface

DOI: 10.1021/jacs.5b07806
J. Am. Chem. Soc. 2015, 137, 13866−13875

properties were extracted from parameters measurable by exhaustive in situ atomic force microscopy during photoirradiation. Such correlations are not currently available, although they are very important in order to develop mathematical models to quantitatively describe these effects in the future.

It is concluded that the type of photomechanical response, classified as four kinematic effects (cracking, hopping, splitting, and bending), depends on the aspect ratio of the crystals, among other factors. At the surface of the crystals studied here, the average force of adhesion gradually decreases, whereas the surface energy gradually increases with the photodimerization. This causes shrinking of the surface layer along preferred direction that correlates with a decrease of the intermolecular distance during dimerization, which ultimately results in surface striations and eventually in delamination by curling of strips off the crystal surface. Macroscopic shrinking by deeper penetration of the light from one side of the crystal in elongated crystals causes visible bending. In blocky crystals, on the other hand, the irradiation causes splintering and explosion, which appears as hopping of the crystals (photosalient effect, PSE). Unlike the bending, it is extremely difficult to quantify the PSE, because in most cases the crystals splinter in highly unpredictable, stochastic manner, making extraction of even basic parameters, such as kinetic energy of the debris, practically impossible. The dependence of the PSE on both deterministic (e.g., conversion yield, crystal size, spatial distribution of product, photon flux) and stochastic factors (various crystal defects) turns the events that lead to the occurrence of this effect highly unpredictable. Particularly the role of defects that are present even in high-quality (real) single crystals adds to the uncertainty in predicting the dependence of these effects on a single intrinsic or external factor, even when the other factors are potentially and in principle controllable. In the related TSE, twinning, which could be considered as a "defect interface", notably decreases the temperature of the effect.[44] This result highlights the critical role of the defects on these events. Therefore, direct correlation of the onset of the effect with the conversion yield, for example, would be a futile exercise. The results of our photodiffraction experiments set 12.5% (at least for crystals of several hundred microns) as approximate *lower limit* of the range of conversion yields that a single crystal can withstand *without undergoing* PSE, that is, crystals of this compound can tolerate at least 12.5% conversion without exploding. In summary, this work demonstrates that a single material can display multiple photomechanical effects, the type of the effect depending on the interplay of a number of controllable and random factors. Together, the results provide better understanding of the reasons for the occurrence of the mechanical effects, although the stochastic nature of some of these effects remains out of the experimenter's control.

4. EXPERIMENTAL METHODS

4.1. Materials and Crystallization. *E*-BDHF was obtained from a chemical company as custom-made product and was purified by recrystallization. All solvents were from Sigma-Aldrich. Single crystals of *E*-BDHF were obtained by slow evaporation from solutions prepared by dissolving ∼10 mg of the compound in nearly hundred pure solvents and solvent mixtures. Single crystals of good quality were selected from the crystallized batches (see Table S1, Supporting Information). Long crystals with plate- or needle-like morphology were obtained by sublimation at 60 °C under reduced pressure. The sublimation was carried out in a sublimation apparatus with a coldfinger maintained at low temperature by a continuous water flow. Single crystal of $(E\text{-BDHF})_{0.875}(0.5c\textit{E}\text{-BDHF})_{0.125}$ was obtained by irradiating a good quality single crystal of *E*-BDHF glued to a glass fiber with six LED lights of wavelength 365 nm for 24 h. The pure product dimer c*E*-BDHF was obtained by exposing 20 mg of *E*-BDHF to high-power UV light from a medium-pressure mercury lamp for 5−10 min. The product was recrystallized by slow evaporation from toluene solution to obtain blocky crystals of the product.

4.2. Single Crystal X-ray Diffraction. Single crystal X-ray diffraction analyses of *E*-BDHF, $(E\text{-BDHF})_{0.875}(0.5c\textit{E}\text{-BDHF})_{0.125}$, and c*E*-BDHF were carried out using a Bruker APEX DUO[62] diffractometer with CCD area detector and monochromatic Mo$K\alpha$ radiation (λ = 0.71069 Å). Crystals of *E*-BDHF and c*E*-BDHF were attached to a loop and crystal of $(E\text{-BDHF})_{0.875}(0.5c\textit{E}\text{-BDHF})_{0.125}$ was glued to a glass fiber. The data collection for *E*-BDHF was carried out at 150 and 298 K. The data for $(E\text{-BDHF})_{0.875}(0.5c\textit{E}\text{-BDHF})_{0.125}$ and c*E*-BDHF were collected at 150 K. The data were integrated, scaled, and corrected for absorption with SADABS using the multiscan method.[63] The structures were solved with direct methods with SHELXS-97[64] and refined with SHELXL-2014.[65] All hydrogens attached to carbon atoms were placed at calculated positions and the non-hydrogen atoms in *E*-BDHF and c*E*-BDHF were refined anisotropically. The disorder in $(E\text{-BDHF})_{0.875}(0.5c\textit{E}\text{-BDHF})_{0.125}$ was modeled by using the PART, FVAR, and SAME commands. The non-hydrogen atoms of the minor component were refined isotropically, whereas those of the major component were refined anisotropically.

4.3. Powder X-ray Diffraction. High-resolution X-ray powder diffraction patterns were collected on a D8 Advance laboratory powder diffractometer [Bruker, Cu$K\alpha_1$, radiation from primary Ge(111)-Johannson-type monochromator, Vån-tag-1 position sensitive detector (PSD), with an opening angle of 6°] in Debye−Scherrer geometry. Prior to the measurement the samples were manually powdered in a mortar and pestle and sealed in borosilicate glass capillaries of 0.5 mm diameter (Hilgenberg glass No. 50). The samples were spun during data collection for better particle statistics. The TOPAS 4.2.[66] program was used for the Rietveld refinements.[67] The single crystal structures of the monomer and the dimer were used as model structures. All profile, lattice and structural parameters were subjected to free unconstrained refinement. The final plots are shown in Figure S4, Supporting Information. The anisotropy of width and asymmetry of the Bragg reflections were modeled by applying symmetry adapted spherical harmonics of low order, which were convoluted with geometrical and instrumental contributions to the final peak profile. For the in situ photodiffraction experiments a custom-made photocell was mounted on the diffractometer.[54] Powder patterns were collected every 5 min during continuous irradiation with high-intensity UV light. The 11−13° Bragg angle region was selected, and the intensities of the (101) reflections from the monomer and the dimer were followed.

4.4. Kinematic Analysis. Single crystals of *E*-BDHF were exposed to UV light (365 nm) from a medium-pressure mercury lamp (SP-7, Ushio) equipped with internal heat filter. The light output was inclined to the base at an angle of ∼60° and placed at a distance of 5 cm from the crystals. Before the exposure to UV light still photographs of each crystal were recorded to extract their dimensions (l, w, t). Each dimension

DOI: 10.1021/jacs.5b07806
J. Am. Chem. Soc. 2015, 137, 13866−13875

was calculated as an average of three independent measurements at three different positions of the crystal. The mechanical effects of the crystals observed during the exposure to UV light were recorded with a high-speed camera HotShot 1280 CC (frame rate: 4000 s^{-1}) mounted on a Nikon SMZT trinocular reflection-type stereoscope. The photomechanical bending or twisting of the (sublimed) crystals was recorded with a normal digital camera mounted on a Nikon transmission-type microscope SMZ1500. The crystals were glued at one end to a thin glass fiber and one of the wide faces was exposed to UV light from a medium pressure mercury lamp placed at a distance 5 cm from the crystal.

4.5. Scanning Electron Microscopy (SEM). FEI Quanta 450 Field Emission scanning electron microscope was used to study the surface morphology of the crystals before and after UV irradiation. A working distance of 9.8 mm was used. The samples were coated with gold before examination.

4.6. Atomic Force Microscopy (AFM). For qualitative inspection, the AFM observations were carried out with Witec Alpha 300 confocal Raman/AFM at NYUAD. The AFM was used in AC contact (tapping mode). The cantilevers were operated at resonance (~80 kHz) and the cantilever tips had a nominal tip radius of ~15 nm. Typical scans were over an area of 5 by 5 μm with 512 by 512 points measured. Feedback settings were optimized for each image scan. The quantitative experiments were carried out at the Masdar Institute with Cypher AFM from Asylum Research and standard Olympus cantilevers (AC160TS). The AFM force measurement was conducted in amplitude modulation mode. The tip−sample force was recovered by using the Sader−Jarvis Katan formlism,[68] as explained in detail elsewhere.[69] Experimental observables were recorded for force reconstruction including the tip oscillation amplitude (A) and phase shift (Φ) as a function of the tip−sample separation d

$$F_{ts}(d) = 2k\int_{u=d}^{u=\infty}\left[\left(1+\frac{A^{1/2}(u)}{8\sqrt{\pi(u-d)}}\right)\Omega(u) - \frac{A^{3/2}(u)}{\sqrt{2(u-d)}}\frac{d\Omega(u)}{du}\right]du \quad (2)$$

where Ω is the normalized frequency shift expressed as

$$\Omega(d) = \left[1+\frac{A_0}{QA}\cos(\Phi(d))\right]^{1/2} - 1 \quad (3)$$

In eq 3, Q is the quality factor which can be obtained by performing standard thermal analysis at tip−sample separation of 30 nm, and A_0 is the free amplitude of the tip. In this work, the free amplitude of ~40 nm was used in order to avoid bistability. The standard deviations and average values were calculated from 1000 force curves acquired for different UV exposure time.

■ ASSOCIATED CONTENT

Supporting Information

These materials are available via the Internet at The Supporting Information is available free of charge on the ACS Publications website at DOI: 10.1021/jacs.5b07806.

Optical and AFM images of *E*-BDHF crystals before and after irradiation, powder diffraction patterns, reaction cavities, crystal packing, and plots of the tip−sample force curve, surface energy and adhesion force. Tables with kinematic parameters, basic crystallographic data and refinement parameters. (PDF)

Photosalient effect of crystals of *E*-BDHF. (AVI)

Kinematic effect 1 (crystals remain still when exposed to UV light). (AVI)

Kinematic effect 2 (crystals jump without splitting). (AVI)

Kinematic effect 2 (crystals jump without splitting). (AVI)

Kinematic effect 3 (crystals split into pieces that fly off in opposite directions). (AVI)

Kinematic effect 3 (crystals split into pieces that fly off in opposite directions). (AVI)

Kinematic effect 3 (crystals split into pieces that fly off in opposite directions). (AVI)

Kinematic effect 3 (crystals split into pieces). Upon prolonged exposure to UV light, the pieces split to smaller pieces. (AVI)

Kinematic effect 4 (crystals first bend and then split into two or more pieces). (AVI)

Thin crystal affixed to a glass fiber at one end bends when exposed to UV light. Further irradiation results in splitting of the crystal. (AVI)

UV irradiation of a layered crystal affixed at one end to a glass fiber results in separation of the layers, followed by bending and twisting. (AVI)

CIF of *E*-BDHF crystal structure at 150 K. (CIF)

CIF of *E*-BDHF crystal structure at 298 K. (CIF)

CIF of the crystal structure of $(E\text{-BDHF})_{0.875}$(0.5c*E*-BDHF)$_{0.125}$, the partially converted crystal at 150 K. (CIF)

CIF of c*E*-BDHF crystal structure at 150 K. (CIF)

IUCr Checkcif report of $(E\text{-BDHF})_{0.875}$(0.5c*E*-BDHF)$_{0.125}$.(PDF)

IUCr Checkcif report of *E*-BDHF at 150 K. (PDF)

IUCr Checkcif report of *E*-BDHF at 298 K. (PDF)

IUCr Checkcif report of c*E*-BDHF at 150 K. (PDF)

■ AUTHOR INFORMATION

Corresponding Author

*E-mail: pance.naumov@nyu.edu. Tel.: +971-(0)2-628-4572. Fax: +971-(0)2-628-8616.

Author Contributions

The manuscript was written through contributions of all authors. All authors have given approval to the final version of the manuscript.

Notes

The authors declare no competing financial interest.

■ ACKNOWLEDGMENTS

We thank New York University for the financial support of this work. We thank James Weston (NYUAD) for his help with the AFM experiments. This research was partially carried out using Core Technology Platform resources at New York University Abu Dhabi.

■ REFERENCES

(1) Juodkazis, S.; Mukai, N.; Wakaki, R.; Yamaguchi, A.; Matsuo, S.; Misawa, H. *Nature* **2000**, *408*, 178−181.

(2) Yu, Y.; Nakano, M.; Ikeda, T. *Nature* **2003**, *425*, 145.

(3) Ikeda, T.; Mamiya, J.-i.; Yu, Y. *Angew. Chem., Int. Ed.* **2007**, *46*, 506−528.

(4) Wei, J.; Yu, Y. *Soft Matter* **2012**, *8*, 8050−8059.
(5) Nath, N. K.; Panda, M. K.; Sahoo, S. C.; Naumov, P. *CrystEngComm* **2014**, *16*, 1850−1858.
(6) Nath, N. K.; Pejov, L.; Nichols, S. M.; Hu, C.; Saleh, N.; Kahr, B.; Naumov, P. *J. Am. Chem. Soc.* **2014**, *136*, 2757−2766.
(7) Naumov, P.; Kowalik, J.; Solntsev, K. M.; Baldridge, A.; Moon, J.-S.; Kranz, C.; Tolbert, L. M. *J. Am. Chem. Soc.* **2010**, *132*, 5845−5857.
(8) Koshima, H.; Ojima, N.; Uchimoto, H. *J. Am. Chem. Soc.* **2009**, *131*, 6890−6891.
(9) Koshima, H.; Ojima, N. *Dyes Pigm.* **2012**, *92*, 798−801.
(10) Koshima, H.; Takechi, K.; Uchimoto, H.; Shiro, M.; Hashizume, D. *Chem. Commun.* **2011**, *47*, 11423−11425.
(11) Sun, J.-K.; Li, W.; Chen, C.; Ren, C.-X.; Pan, D.-M.; Zhang, J. *Angew. Chem., Int. Ed.* **2013**, *52*, 6653−6657.
(12) Bushuyev, O. S.; Singleton, T. A.; Barrett, C. J. *Adv. Mater.* **2013**, *25*, 1796−1800.
(13) Bushuyev, O. S.; Tomberg, A.; Friščić, T.; Barrett, C. J. *J. Am. Chem. Soc.* **2013**, *135*, 12556−12559.
(14) Stolow, R. D.; Larsen, J. W. *Chem. Ind.* **1963**, *449*, 326−327.
(15) Uchida, K.; Sukata, S.-J.; Matsuzawa, Y.; Akazawa, M.; de Jong, J. J. D.; Katsonis, N.; Kojima, Y.; Nakamura, S.; Areephong, J.; Meetsma, A.; Feringa, B. L. *Chem. Commun.* **2008**, 326−328.
(16) Kim, T.; Al-Muhanna, M. K.; Al-Suwaidan, S. D.; Al-Kaysi, R. O.; Bardeen, C. J. *Angew. Chem., Int. Ed.* **2013**, *52*, 6889−6893.
(17) Zhu, L.; Al-Kaysi, R. O.; Bardeen, C. J. *J. Am. Chem. Soc.* **2011**, *133*, 12569−12575.
(18) Kim, T.; Zhu, L.; Mueller, L. J.; Bardeen, C. J. *CrystEngComm* **2012**, *14*, 7792−7799.
(19) Shtukenberg, A. G.; Freudenthal, J.; Kahr, B. *J. Am. Chem. Soc.* **2010**, *132*, 9341−9349.
(20) Kitagawa, D.; Nishi, H.; Kobatake, S. *Angew. Chem., Int. Ed.* **2013**, *52*, 9320−9322.
(21) Kim, T.; Zhu, L.; Mueller, L. J.; Bardeen, C. J. *J. Am. Chem. Soc.* **2014**, *136*, 6617−6625.
(22) Natarajan, A.; Tsai, C. K.; Khan, S. I.; McCarren, P.; Houk, K. N.; Garcia-Garibay, M. A. *J. Am. Chem. Soc.* **2007**, *129*, 9846−9847.
(23) Commins, P.; Natarajan, A.; Tsai, C.-K.; Khan, S. I.; Nath, N. K.; Naumov, P.; Garcia-Garibay, M. A. *Cryst. Growth Des.* **2015**, *15*, 1983−1990.
(24) Colombier, I.; Spagnoli, S.; Corval, A.; Baldeck, P. L.; Giraud, M.; Leaustic, A.; Yu, P.; Irie, M. *J. Chem. Phys.* **2007**, *126*, 011101.
(25) Naumov, P.; Sahoo, S. C.; Zakharov, B. A.; Boldyreva, E. V. *Angew. Chem., Int. Ed.* **2013**, *52*, 9990−9995.
(26) Medishetty, R.; Husain, A.; Bai, Z.; Runčevski, T.; Dinnebier, R. E.; Naumov, P.; Vittal, J. J. *Angew. Chem., Int. Ed.* **2014**, *53*, 5907−5911.
(27) Medishetty, R.; Sahoo, S. C.; Mulijanto, C. E.; Naumov, P.; Vittal, J. J. *Chem. Mater.* **2015**, *27*, 1821−1829.
(28) Ghosh, S.; Mishra, M. K.; Ganguly, S.; Desiraju, G. R. *J. Am. Chem. Soc.* **2015**, *137*, 9912−9921.
(29) Uchida, E.; Azumi, R.; Norikane, Y. *Nat. Commun.* **2015**, *6*, 7310.
(30) Kole, G. K.; Vittal, J. J. *Chem. Soc. Rev.* **2013**, *42*, 1755−1775.
(31) Park, I.-H.; Chanthapally, A.; Zhang, Z.; Lee, S. S.; Zaworotko, M. J.; Vittal, J. J. *Angew. Chem., Int. Ed.* **2014**, *53*, 414−419.
(32) Garai, M.; Santra, R.; Biradha, K. *Angew. Chem., Int. Ed.* **2013**, *52*, 5548−5551.
(33) Bhogala, B. R.; Captain, B.; Parthasarathy, A.; Ramamurthy, V. *J. Am. Chem. Soc.* **2010**, *132*, 13434−13442.
(34) Mondal, B.; Captain, B.; Ramamurthy, V. *Photochem. Photobiol. Sci.* **2011**, *10*, 891−894.
(35) Yang, S.-Y.; Deng, X.-L.; Jin, R.-F.; Naumov, P.; Panda, M. K.; Huang, R.-B.; Zheng, L.-S.; Teo, B. K. *J. Am. Chem. Soc.* **2014**, *136*, 558−561.
(36) Yang, S.-Y.; Naumov, P.; Fukuzumi, S. *J. Am. Chem. Soc.* **2009**, *131*, 7247−7249.
(37) Hutchins, K. M.; Rupasinghe, T. P.; Ditzler, L. R.; Swenson, D. C. J.; Sander, R. G.; Baltrusaitis, J.; Tivanski, A. V.; MacGillivray, L. R. *J. Am. Chem. Soc.* **2014**, *136*, 6778−6781.
(38) Papaefstathiou, G. S.; Duncan, A. J. E.; MacGillivray, L. R. *Chem. Commun.* **2014**, *50*, 15960−15962.
(39) Ghorai, S.; Sumrak, J. C.; Hutchins, K. M.; Bučar, D.-K.; Tivanski, A. V.; MacGillivray, L. R. *Chem. Sci.* **2013**, *4*, 4304−4308.
(40) Dutta, S.; Bučar, D.-K.; Elacqua, E.; MacGillivray, L. R. *Chem. Commun.* **2013**, *49*, 1064−1066.
(41) MacGillivray, L. R.; Papaefstathiou, G. S.; Friščić, T.; Hamilton, T. D.; Bučar, D.-K.; Chu, Q.; Varshney, D. B.; Georgiev, I. G. *Acc. Chem. Res.* **2008**, *41*, 280−291.
(42) Kaupp, G.; Haak, M. *Angew. Chem., Int. Ed. Engl.* **1996**, *35*, 2774−2777.
(43) Kearsley, S. K.; Desiraju, G. R. *Proc. R. Soc. London, Ser. A* **1985**, *397*, 157−181.
(44) Sahoo, S. C.; Panda, M. K.; Nath, N. K.; Naumov, P. *J. Am. Chem. Soc.* **2013**, *135*, 12241−12251.
(45) Sahoo, S. C.; Sinha, S. B.; Kiran, M. S. R. N.; Ramamurty, U.; Dericioglu, A. F.; Reddy, C. M.; Naumov, P. *J. Am. Chem. Soc.* **2013**, *135*, 13843−13850.
(46) Panda, M. K.; Runčevski, T.; Sahoo, S. C.; Belik, A. A.; Nath, N. K.; Dinnebier, R. E.; Naumov, P. *Nat. Commun.* **2014**, *5*, 4811.
(47) Avrami, M. *J. Chem. Phys.* **1939**, *7*, 1103−1112.
(48) Johnson, W. A.; Mehl, P. A. *Trans. Am. Inst. Min., Metall., Pet. Eng., Soc. Min. Eng. AIME* **1939**, *135*, 416−458.
(49) Kolmogorov, A. N. *Bull. Acad. Sci. USSR, Phys. Ser.* **1937**, *1*, 355−359.
(50) Moré, R.; Busse, G.; Hallmann, J.; Paulmann, C.; Scholz, M.; Techert, S. *J. Phys. Chem. C* **2010**, *114*, 4142−4148.
(51) Schmidt, G. M. *Pure Appl. Chem.* **1971**, *27*, 647−678.
(52) Ohashi, Y.; Yanagi, K.; Kurihara, T.; Sasada, Y.; Ohgo, Y. *J. Am. Chem. Soc.* **1981**, *103*, 5805−5812.
(53) Kodama, S.; Johmoto, K.; Sekine, A.; Fujii, K.; Uekusa, H. *CrystEngComm* **2013**, *15*, 4667−4675.
(54) Runčevski, T.; Blanco-Lomas, M.; Marazzi, M.; Cejuela, M.; Sampedro, D. D.; Dinnebier, R. E. *Angew. Chem., Int. Ed.* **2014**, *53*, 6738−6742.
(55) Isreaelchvili, J. N. *Intermolecular and Surface Forces*, 3rd ed.; Elsevier: Waltham, MA, 2011.
(56) Yaminsky, V. V. *Colloids Surf., A* **1999**, *159*, 181−195.
(57) Derjaguin, B. V.; Muller, V. M.; Toporov, Y. P. *J. Colloid Interface Sci.* **1975**, *53*, 314−326.
(58) Karunatilaka, C.; Krešimir-Bučar, D.; Ditzler, L. R.; Friščić, T.; Swenson, D. C.; MacGillivray, L. R.; Tivanski, A. V. *Angew. Chem., Int. Ed.* **2011**, *50*, 8642−8646.
(59) Santos, S.; Amadei, C. A.; Verdaguer, A.; Chiesa, M. *J. Phys. Chem. C* **2013**, *117*, 10615−10622.
(60) Santos, S.; Guang, L.; Souier, T.; Gadelrab, K.; Chiesa, M.; Thomson, N. H. *Rev. Sci. Instrum.* **2012**, *83*, 043707.
(61) Chang, Y.-H.; Olukan, T.; Lai, C.-Y.; Santos, S.; Lin, T.-Y.; Apostoleris, H.; Font, J.; Barcons, V.; Chiesa, M. *J. Phys. Chem. C* **2015**, *119*, 18267.
(62) *APEX DUO, version 2.1−4, and SAINT, version 7.34A*; Bruker AXS Inc.: Madison, WI, 2012.
(63) Sheldrick, G. M. *SADABS*; University of Göttingen: Göttingen, Germany, 1996.
(64) Sheldrick, G. M. *Acta Crystallogr., Sect. A: Found. Crystallogr.* **2008**, *64*, 112−122.
(65) Sheldrick, G. M. *SHELXL2014*; University of Göttingen: Göttingen, Germany, 2014.
(66) *TOPAS*, version 4.2; Bruker AXS: Billerica, MA, 2007.
(67) Rietveld, H. M. *J. Appl. Crystallogr.* **1969**, *2*, 65−71.
(68) Katan, A. J.; van Es, M. H.; Oosterkamp, T. H. *Nanotechnology* **2009**, *20*, 165703.
(69) Amadei, C. A.; Santos, S.; Pehkonen, S. O.; Verdaguer, A.; Chiesa, M. *J. Phys. Chem. C* **2013**, *117*, 20819−20825.

DOI: 10.1021/jacs.5b07806
J. Am. Chem. Soc. 2015, 137, 13866−13875